On the surface chemisorption of oxidizing fine iron particles: Insights gained from molecular dynamics simulations

Leon C. Thijs[a], Efstratios M. Kritikos[b], Andrea Giusti[b], Giel Ramaekers[a], Jeroen A. van Oijen[a], Philip de Goey[a], XiaoCheng Mi[a,*]

[a] Department of Mechanical Engineering, Eindhoven University of Technology, P.O. Box 513, Eindhoven, NL-5600 MB, the Netherlands
[b] Department of Mechanical Engineering, Imperial College London, London SW7 2AZ, United Kingdom

A B S T R A C T

Molecular dynamics (MD) simulations are performed to investigate the thermal and mass accommodation coefficients (TAC and MAC, respectively) for the combination of iron(-oxide) and air. The obtained values of TAC and MAC are then used in a point-particle Knudsen model to investigate the effect of chemisorption and the Knudsen transition regime on the combustion behavior of (fine) iron particles. The thermal accommodation for the interactions of Fe with N_2 and Fe_xO_y with O_2 is investigated for different surface temperatures, while the mass accommodation coefficient for iron(-oxide) with oxygen is investigated for different initial oxidation stages Z_O, which represents the molar ratio of $O/(O + Fe)$, and different surface temperatures. The MAC decreases fast from unity to 0.03 as Z_O increases from 0 to 0.5 and then diminishes as Z_O further increases to 0.57. By incorporating the MD-informed accommodation coefficients into the single iron particle combustion model, the oxidation beyond $Z_O = 0.5$ (from stoichiometric FeO to Fe_3O_4) is modeled. A new temperature evolution for single iron particles is observed compared to results obtained with previously developed continuum models. Specifically, results of the present simulations show that the oxidation process continues after the particle reaching the peak temperature, while previous models predicting that the maximum temperature was attained when the particle is oxidized to $Z_O = 0.5$. Since the rate of oxidation slows down as the MAC decreases with an increasing oxidation stage, the rate of heat loss exceeds the rate of heat release upon reaching the maximum temperature, while the particle is not yet oxidized to $Z_O = 0.5$. Finally, the effect of transition-regime heat and mass transfer on the combustion behavior of fine iron particles is investigated and discussed.

1. Introduction

Iron powder is considered as a promising metal fuel since it is inherently carbon-free, recyclable, compact, cheap and widely available [2]. To design and improve real-world iron-fuel burners, an in-depth understanding of the fundamentals underlying the combustion of fine iron particles is required.

Over the past five years, the interest in using iron powder as a circular carrier of renewable energy has drastically increased. McRae et al. [22], Soo et al. [36], Tang et al. [39], Tóth et al. [44] and Li et al. [19] performed experiments with iron dust flames to study fundamental characteristics of iron combustion, such as flame structure and flame propagation. Tóth et al. [44] and Li

et al. [19] identified the formation of nano-particles in their experiments, where they observed halos of nano-particles surrounding the burning iron particles. To gain a more in-depth understanding of the oxidation processes of iron particles, the canonical configuration of single iron particle combustion has been investigated by multiple researchers. Ning et al. [26,27] performed single particle combustion experiments where the particles are ignited by a laser. They showed that the duration of burning process is sensitive to the surrounding oxygen concentration. They also observed that the maximum particle temperature increases with gas-phase oxygen concentration while reaching a plateau at sufficiently elevated oxygen concentrations. Formation of oxide nano-particles during the combustion was also recorded. Li et al. [18] investigated the ignition and combustion process of single micron-sized iron particles in the hot gas flow of a burned methane-oxygen-nitrogen mixture, and drew similar conclusions as Ning et al. [26]. Panahi et al. [28] used a drop-tube furnace to burn iron particles at a high gas

---

* Corresponding author.
E-mail address: x.c.mi@tue.nl (X. Mi).

temperature ($\approx$ 1350 K) with oxygen concentrations of 21%, 50% and 100%. They showed that particle temperature increases significantly when the oxygen concentration increases from 21% to 50%, but barely further increases when increasing from 50% to 100%.

In the past few years, the number of theoretical models for single iron particles has increased. Mi et al. [23] investigated the ignition behavior of iron particles via solid-phase oxidation kinetics described by a parabolic rate. Jean-Philyppe et al. [15] extended this model and investigated the ignition behavior of fine iron particles in the Knudsen transition regime. They stated that the transition effect on the ignition characteristics becomes important if the particle diameter is below 30 μm. Senyurt and Dreizin [31] studied the ignition of metal particles other than iron in the transition regime, and stated that transition effects could always be neglected for very large (i.e., > 200 μm) particles. While these models only focused on the ignition, Soo et al. [35] developed a generic model for the full combustion behavior for non-volatile solid-fuel particles, wherein the particle oxidation rate depends on reaction kinetics at the surface of the particle and the external diffusion of oxygen to the particle. Hazenberg and van Oijen [13] further extended this model by taking into account the growth of the particle during oxidation. In [41], a boundary layer resolved model was developed so that mass and heat transfer are accurately modeled, including Stefan flow. Temperature-dependent properties were used for the gas- and condensed-phase species and evaporation was implemented to investigate the formation of nano-sized iron-oxides products. It was shown that, although the particle temperature remains below the boiling point of iron(-oxide), a non-negligible amount of iron mass is lost due to the evaporation of the particle. Furthermore, it was shown that when only the conversion of Fe to FeO is considered up to the maximum temperature, and when internal transport is neglected, a good agreement was obtained with the experimental data of Ning et al. [27] for the combustion time and maximum temperature as a function of oxygen concentration. The further oxidation after the particle peak temperature was, however, not modeled. In a later work of Thijs et al. [40], the point-particle model of Hazenberg and van Oijen [13] was extended, with aid of a boundary-layer-resolved model, to include temperature-dependent properties, slip velocity, Stefan flow, and evaporation. van Gool et al. [12] extended the latter particle model and modeled the particle composition as being uniform and in thermodynamic equilibrium, enabling the oxidation beyond stoichiometric FeO.

For iron particle combustion, it has been hypothesized that the oxidation rate of an iron droplet is the result of an interplay among three mechanisms: (1) External diffusion of O_2 from the ambient gas to particle surface, (2) surface chemisorption of O_2, and (3) internal transport of Fe and O atoms [38]. In the previously discussed numerical models, it assumed that mechanism (1) is the rate limiting step, and that mechanisms (2) and (3) are infinitely fast. However, these assumptions are not well investigated. Furthermore, in most of the previously discussed models for iron-particle combustion, the continuum assumption is used to describe the transport processes. It is known that, when the size of the particle becomes too small, modeling the heat and mass transfer using the continuum approach becomes invalid. The particle radius, r_p, compared to the mean free path length of the gas molecules, λ_{MFP}, is described by the Knudsen number [20]

$$\text{Kn} = \lambda_{MFP}/r_p. \tag{1}$$

Typically, when Kn is larger than 0.01 [20], the continuum approach is invalid. An elaborate review of modeling heat transfer in the transition regime for nano-particles in the context of laser-induced incandescence is presented by Liu et al. [20]. In the previous study of Thijs et al. [41], only relatively large particles of 40 and 50 μm were considered, ensuring that the transition-regime

heat and mass transfer has a negligible effect. While [15] and [31] studied the transition effect on the ignition behavior of metal particles, such a study was not performed for the complete combustion process of single iron particles.

The heat and mass transfer in the free-molecular regime is dependent on the thermal and mass accommodation coefficients. The average energy transfer when gas molecules scatter from the surface is described by the thermal accommodation coefficient (TAC). The mass accommodation coefficient (MAC) or absorption coefficient is defined as the fraction of incoming oxygen molecules that are absorbed (accommodated) rather than reflected when they collide with the iron surface. Molecular dynamics simulation can be used to investigate these accommodation coefficients. Multiple studies have been performed with molecular dynamics simulations to investigate the metal surface-gas interactions. In the case of highly-rarefied gases (Kn > 10), the interaction between one gas molecule and the surface is considered. Chirita et al. [4] performed one of the pioneering studies that consider molecular beam simulations to simulate incident low energy argon molecules on a nickel surface. Later, multiple authors [6,7,21,29,32,33,43] investigated the gas-surface interactions, considering one gas molecules issuing from a Maxwell–Boltzmann distribution. [7] showed that the TAC obtained with such a molecular dynamics simulation well agrees with experimental data. In less rarefied gases (Kn < 1) gas-gas interactions become important in addition to the surface-gas interactions, and can impact the accommodation coefficients [10,25,37]. Alas, to the authors' knowledge, a systematic analysis of the TAC and MAC for a system of iron(-oxide) surface exposed to air has not yet been reported. Such a study of the MAC is also of importance to derive effective chemical kinetics governing the rate of further oxidation beyond the stoichiometry of FeO, which are missing in literature.

To study the effect of chemisorption and the effect of the free-molecular regime, molecular dynamics simulations are performed to determine the TAC and MAC for an iron(-oxide)-air system. Then, these values are used in a two-layer point-particle model to examine the effect of chemisorption and the effect of the Knudsen transition regime on the combustion behavior of single iron particles. The paper is organized as follows. Section 2 describes the methodology of the two-layer model used to describe the combustion of single iron particles. In Section 3, the procedure for the molecular dynamics simulations used to determine the thermal and mass accommodation coefficients is discussed. Section 4 presents the results of the TAC and MAC obtained from these molecular dynamics simulations. In Section 5, the results of the single iron particle combustion model are discussed. Conclusions are provided in Section 6.

## 2. Model formulation for single iron particle combustion

In the current study, a two-layer point-particle model is used as shown in Fig. 1. An iron particle oxidation model is coupled to a two-layer method to take into account the Knudsen transition regime. The iron particle oxidation model assumes a homogeneous mixture of iron and oxygen and is based on the previous work [40].

In [40], only the oxidation from Fe into FeO was taken into account via

$$R1: Fe + \frac{1}{2}O_2 \rightarrow FeO. \tag{2}$$

Here, the oxidation mechanism is extended by considering the further oxidation into Fe_3O_4. Once all the Fe is converted into FeO, the FeO continues to oxidize into Fe_3O_4 via

$$R2: 3FeO + \frac{1}{2}O_2 \rightarrow Fe_3O_4. \tag{3}$$
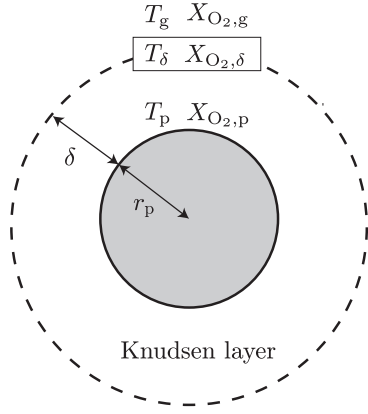
Fig. 1. The configuration for heat and mass transfer analysis considered in the Knudsen model.

The oxidation into Fe_2O_3 is not considered since the re-solidification process is rather complex. Furthermore, the impact of the oxidation from Fe_3O_4 into Fe_2O_3 is rather small since only 10% of the total energy is released in this step. Based on the thermodynamics of the Fe-O system [14], it is known that iron-oxide can be formed in multiple crystalline structures, i.e., FeO (wustite), Fe_3O_4 (magnetite), and Fe_2O_3 (hematite). In the liquid phase of an Fe–O mixture, there are no clear crystalline structures. This region on the Fe–O phase diagram consists mainly of two different liquids denoted by L1 (iron) and L2 (iron-oxide). Therefore, considering these phases as "liquid FeO" and "liquid Fe_3O_4" is not in line with the phase diagram.

The thermodynamic data for the L1 and L2 mixture are, however, unknown. In this work, the thermodynamic data for the L1 and L2 mixtures are therefore approximated to be a linear combination of the liquid-phase data of Fe, FeO, and Fe_3O_4. The total enthalpy of a liquid iron particle, $H_{liq,tot}$, is determined via

$$H_{liq,tot} = m_{Fe}h_{Fe} + m_{FeO}h_{FeO} + m_{Fe_3O_4}h_{Fe_3O_4},\qquad(4)$$

with, m_i the mass of species i in the particle and h_i the mass specific enthalpy of species i (calculated with the NASA polynomials). The liquid-phase polynomials are extrapolated to the boiling point of FeO ($T_p = 3396\,K$).

The phase diagram of the Fe-O system is dependent on the molar ratio of $O/(O + Fe)$, which defines the oxidation stage of the (liquid) iron particle. Here, this ratio is denoted by Z_O, which is the elemental mole fraction of oxygen in the particle, and is defined as

$$Z_O = \frac{m_{O,p}/M_O}{m_{Fe,p}/M_{Fe} + m_{O,p}M_{Fe}},\qquad(5)$$

where $m_{O,p}$ is the mass of oxygen, $m_{Fe,p}$ the total mass of iron in the particle, and M_O and M_{Fe} are the molar mass of oxygen and iron, respectively. In this work, Z_O denotes the oxidation stage of the iron particle, where $Z_O = 0.5$ represents "liquid FeO" and $Z_O = 0.57$ "liquid Fe_3O_4".

To calculate the total enthalpy of the particle, the rates of change of m_{Fe}, m_{FeO}, and $m_{Fe_3O_4}$ need to be tracked. Since the equilibrium vapor pressure calculated with the thermodynamic data of liquid Fe_3O_4 is orders-of-magnitude lower than those of liquid Fe and FeO [27], evaporation of Fe_3O_4 is negligible compared to the evaporation of Fe and FeO. In [41] it was discussed that the oxidation of the gaseous iron will further inhibit the diffusion of oxygen towards the particle. To include this effect in the current point-particle model, it is taken into account that Fe(g) and FeO(g) will further oxidize and condense into Fe_2O_3. The oxygen consumed by the gaseous iron(-oxide) species will limit the total mass transfer rate of oxygen. The mass transfer rate of oxygen consumed by the

gaseous iron(-oxide) is given as Fujinawa et al. [11]

$$\dot{m}_{O_2,vap} = s_{Fe_2O_3,Fe(g)}\frac{dm_{evap,Fe}}{dt} + s_{Fe_2O_3,FeO(g)}\frac{dm_{evap,FeO}}{dt},\qquad(6)$$

with $s_{Fe_2O_3,Fe(g)}$ and $s_{Fe_2O_3,FeO(g)}$ the stoichiometric mass ratios for the oxidation of respectively Fe(g) and FeO(g) into Fe_2O_3. The rate of change of m_{Fe}, m_{FeO}, and $m_{Fe_3O_4}$ are related to the rate of oxidation and the rate of evaporation via

$$\frac{dm_{Fe}}{dt} = -\frac{1}{s_{Fe,1}}\left(\dot{m}_{O_2,1}-\dot{m}_{O_2,vap}\right) - \frac{dm_{evap,Fe}}{dt},\qquad(7)$$

$$\frac{dm_{FeO}}{dt}\begin{cases}-\dfrac{1}{s_{FeO,1}}\left(\dot{m}_{O_2,1}-\dot{m}_{O_2,vap}\right) - \dfrac{dm_{evap,FeO}}{dt} & \text{if } Z_O < 0.5,\\[2mm] -\dfrac{1}{s_{FeO,2}}\left(\dot{m}_{O_2,2}-\dot{m}_{O_2,vap}\right) - \dfrac{dm_{evap,FeO}}{dt} & \text{if } Z_O > 0.5,\end{cases}\qquad(8)$$

$$\frac{dm_{Fe_3O_4}}{dt} = -\frac{1}{s_{Fe_3O_4,2}}\left(\dot{m}_{O_2,2}-\dot{m}_{O_2,vap}\right),\qquad(9)$$

with $\dot{m}_{O_2,j}$ the mass transfer rate of oxygen to the particle via either reaction R1 (denoted by 1) or R2 (denoted by 2) and $s_{i,j}$ is the stoichiometric mass ratio of species i for reaction j. The total mass transfer rate of oxygen is given by $\dot{m}_{O_2} = \dot{m}_{O_2,1} + \dot{m}_{O_2,2}$. Note that R1 and R2 are sequential reactions in this work, where R2 starts if $Z_O > 0.5$. Therefore, either $\dot{m}_{O_2,1}$ or $\dot{m}_{O_2,2}$ equals zero.

To calculate Z_O, the mass of O and Fe in the particle must be known. The rate of change of O is related to the rate of oxidation and the rate of evaporation of FeO, while the rate of change of m_{Fe} which is in the particle, is only affected by evaporation

$$\frac{dm_{O,p}}{dt} = \dot{m}_{O_2} - \frac{M_O}{M_{FeO}}\frac{dm_{evap,FeO}}{dt},\qquad(10)$$

$$\frac{dm_{Fe,p}}{dt} = -\frac{dm_{evap,Fe}}{dt} - \frac{M_{Fe}}{M_{FeO}}\frac{dm_{evap,FeO}}{dt},\qquad(11)$$

with M_{FeO} the molar mass of FeO. Temperature-dependent density functions are used to relate the mass of the particle to the volume and diameter, see van Gool et al. [12] for the specific polynomials.

The rate of change of the particle enthalpy is described by

$$\frac{dH_p}{dt} = q + q_{rad} + \dot{m}_{O_2}h_{O_2} - \sum_i h_{i,v}\frac{dm_{evap,i}}{dt},\qquad(12)$$

with q the heat transfer rate, q_{rad} the radiative heat transfer rate, h_{O_2} the mass-specific enthalpy of the consumed oxygen and $h_{i,v}$ the mass-specific enthalpy of the evaporated species.

To model the mass transfer rate $\dot{m}_{O_2}$ and heat transfer rate q, a two-layer method is used. Figure 1 illustrates the configuration which is used for the two-layer model. The iron particle is surrounded by a spherical Knudsen layer δ with a thickness equal to the mean free path λ_{MFP} of the gas molecules [20]

$$\lambda_{MFP} = \frac{k_\delta}{p}\frac{\gamma_\delta - 1}{9\gamma_\delta - 5}\sqrt{\frac{8\pi m_{O_2}T_\delta}{k_b}},\qquad(13)$$

with k_δ and γ_δ being the thermal conductivity and specific heat ratio derived at the Knudsen layer, p the ambient pressure, m_{O_2} the mass of an oxygen molecule, and k_b the Boltzmann constant.

At the Knudsen layer, the gas has a temperature T_δ and mole fraction X_δ. In the two-layer method, it is assumed that the heat and mass transfer across the Knudsen layer is quasi-steady [20]. Therefore, the mass balance at $r = \delta$ yields $\dot{m}_{O_2,FM} = \dot{m}_{O_2,c}$, with $\dot{m}_{O_2,FM}$ the mass transfer rate in the free-molecular regime and $\dot{m}_{O_2,c}$ the mass transfer rate in the continuum regime. Similarly, the heat balance can be written as $q_{FM} = q_c$.

The mass transfer rate and heat transfer rate in the continuum regime can be described as Senyurt and Dreizin [31], Thijs et al. [40]

$$\dot{m}_{O_2,c} = 2\pi\,Sh(\delta + r_p)\rho_{O2,f}D_f\left(X_{O_2,g} - X_{O_2,\delta}\right),\qquad(14)$$

$$q_c = 2\pi \, \mathrm{Nu}(\delta + r_p)k_f(T_g - T_\delta), \tag{15}$$

with T_g is the gas temperature, $X_{O_2,g}$ the mole fraction of oxygen in the gas phase, Nu and Sh the Nusselt and Sherwood numbers, respectively and $\rho_{O2,f}$, D_f and k_f the density of oxygen, the mixture-averaged diffusion coefficient and the thermal conductivity derived at the film temperature and composition. To include the effect of a slip velocity and the oxygen consumption induced Stefan flow towards the particle, the Nusselt and Sherwood numbers are corrected by means of the Reynolds number and the mass and heat Spalding numbers. The Stefan flow corrected Nusselt ans Sherwood numbers are determined as

$$\mathrm{Nu} = \mathrm{Nu}^* \ln{(1 + B_T)}/B_T, \tag{16}$$

$$\mathrm{Sh} = \mathrm{Sh}^* \ln{(1 + B_m)}/B_m, \tag{17}$$

with Nu^* and Sh^* being Reynolds number dependent correlations as described in Thijs et al. [40]. The mass Spalding number is defined as Bird et al. [3].

$$B_m = \frac{Y_{O_2,g} - Y_{O_2,p}}{Y_{O_2,p} - 1}. \tag{18}$$

Analogous to the mass Spalding number, a Spalding heat transfer number can be derived as Bird et al. [3].

$$1 + B_T = (1 + B_m)^{\phi_m}, \tag{19}$$

where $\phi_m = \frac{c_{p,\mathrm{ox}}}{c_p} \frac{1}{\mathrm{Le}} \frac{\mathrm{Sh}}{\mathrm{Nu}}$ and $\mathrm{Le} = \frac{\mathrm{Sc}}{\mathrm{Pr}}$ is the Lewis number. A constant slip velocity in time is used, based on the terminal velocity of the iron particle at ambient conditions. For more details of the continuum model, the reader is referred to Thijs et al. [40].

The mass transfer rate in the free-molecular regime can be described as Senyurt and Dreizin [31].

$$\dot{m}_{O_2,\mathrm{FM}} = \alpha_m \pi r_p^2 \nu_\delta \rho_{O2,\delta} X_{O_2,\delta}, \tag{20}$$

with α_m the mass accommodation coefficient and ν_δ the velocity of the gas molecules calculated as

$$\nu_\delta = \sqrt{\frac{8k_b T_\delta}{\pi m_{O_2}}}. \tag{21}$$

Similarly, the heat transfer rate in the free-molecular regime yields [20].

$$q_{\mathrm{FM}} = \alpha_T \pi r_p^2 p \sqrt{\frac{k_b T_\delta}{8\pi m_{O_2}}} \frac{\gamma^* + 1}{\gamma^* - 1} \left(\frac{T_p}{T_\delta} - 1 \right), \tag{22}$$

with α_T the thermal accommodation coefficient and γ^* the averaged specific heat ratio [20]. It is assumed that the slip velocity and Stefan flow do not affect the free-molecular transport and the effect of the transition regime on the evaporation rate is neglected.

To account for the large variation of temperature and composition in the boundary layer, the transport properties are derived at film layer temperature (T_f) and composition (X_f), by using the 1/2 film averaging rule [40]. T_f and X_f are determined via

$$T_f = T_1 + 1/2(T_2 - T_1), \tag{23}$$

$$X_f = X_1 + 1/2(X_2 - X_1). \tag{24}$$

In the Knudsen layer, T_1 and X_1 are the values derived at the particle surface, while T_2 and X_2 are determined at the δ layer. For the continuum layer, T_1 and X_1 are the values derived at the δ layer, while T_2 and X_2 are determined at the far field.

The two-layer method is implicit—a coupled system of nonlinear equations must be solved to find the mass and heat transfer rates. The molar fraction of oxygen $X_{O_2,g}$ and the temperature T_g

in the gas phase are known. Therefore, $X_{O_2,\delta}$ and T_δ remain unknown and should be found via an iterative method. In this work, the lsqnonlin method of MATLAB was used to solve the coupled system of nonlinear equations. The Cantera toolbox was used to calculate the transport properties in the gas phase.

3. Model formulation for molecular dynamics simulations

Molecular dynamics simulations are performed to determine the TAC and MAC for the interactions between a single gas molecule and a iron(-oxide) surface. This is consistent with the free-molecular regime because gas-gas interactions are not considered. Because an N_2 molecule has a strong triple bond, it is unlikely to be chemically absorbed by an iron(-oxide) surface. In the case of NO_x formation, different species like N and NO could possible interact with the iron particle [30]. In this study, only a TAC value for the N_2 molecule in combination with an iron surface is determined, leaving the study of nitrogen oxides for future work. As a result, the Fe-N_2 interactions are modeled using non-reactive potentials. On the contrary, reactive molecular dynamics are considered for the Fe_xO_y-O_2 interactions to compute the TAC and MAC. In reactive MD simulations, statistical and methodological errors can be introduced [17]. In this study, the thermal and mass accommodation coefficients were averaged over a number of instances in order to achieve small statistical uncertainties. Large-scale Atomic/Molecular Massively Parallel Simulator (LAMMPS) [42] is used to perform the molecular dynamics simulations.

3.1. Thermal and mass accommodation coefficients

As previously described, the free-molecular heat transfer rate is dependent on the TAC. The TAC describes the average energy transfer when gas molecules scatter from the surface and is defined as

$$\alpha_T = \frac{\langle E_0 - E_i \rangle}{3k_B(T_s - T_g)}, \tag{25}$$

with $\langle \cdot \rangle$ denoting an ensemble average, E_0 the total energy of the scattered molecule, and E_i the energy of the incident molecule. The denominator represents the maximum energy that could be transferred from the surface to the gas molecule, with T_s the surface temperature and T_g the gas temperature.

The free-molecular mass transfer rate is dependent on the MAC. The MAC or absorption coefficient is defined as the fraction of incoming oxygen molecules that, upon collision with the iron surface, are absorbed (accommodated) rather than reflected. The MAC is defined as

$$\alpha_m = \frac{n_{\mathrm{abs,g}}}{n_{\mathrm{tot,g}}}, \tag{26}$$

with $n_{\mathrm{abs,g}}$ the number of absorbed gas molecules and $n_{\mathrm{tot,g}}$ the total number of gas molecules colliding the surface.

When iron is burned in air, both oxygen and nitrogen may contribute to the total TAC. The thermal accommodation coefficients for Fe with N_2 is independently determined of the interaction between Fe_xO_y with O_2. The ratio between the numbers of collisions of oxygen and nitrogen with the surface is determined by the molar fraction, denoted by X_{O_2}. In the case that an oxygen molecule is accommodated to the surface, it does not contribute to the thermal accommodation coefficient. To account for this effect, the total TAC is calculated as

$$\alpha_{T,\mathrm{tot}} = [1 - X_{O_2}(1 - \alpha_m)]\alpha_{T,N_2} + X_{O_2}(1 - \alpha_m)\alpha_{T,O_2}. \tag{27}$$

Note that if the oxygen molecule is chemically absorbed, the amount of enthalpy possessed by the absorbed oxygen is added to the total internal energy of the particle.
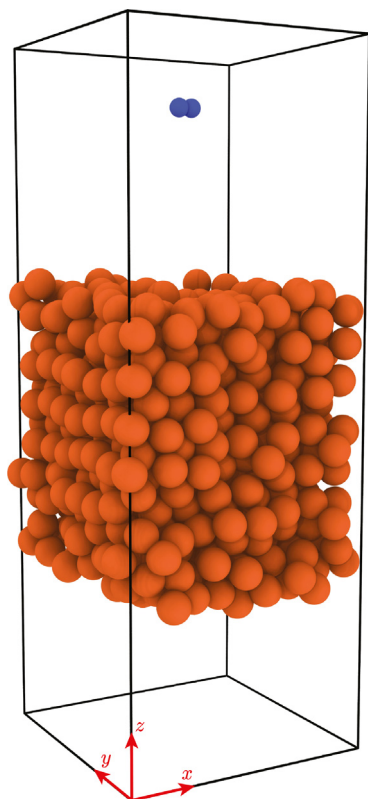
Fig. 2. Initial configuration showing a nitrogen molecule (blue particles) placed above an iron surface (brown particles), with $Z_O = 0$ and $T_p = 2000$ K. The sizes of the particles equal the atomic radii. CPK coloring is used to distinguish different chemical elements.. (For interpretation of the references to colour in this figure legend, the reader is referred to the web version of this article.)

3.2. Fe-N$_2$ interaction

To determine the thermal accommodation coefficients, the procedure as performed by Sipkens and Daun [32] is followed. Figure 2 shows the initial configuration used to determine the thermal accommodation coefficient of the Fe-N$_2$ system. A molecular system is defined with a surface of 686 iron atoms initially arranged in a body-centered cubic (BCC) lattice, with a lattice constant of 2.856 Å, and a nitrogen molecule, of which the latter is modeled as a rigid rotor. The gas molecule is positioned around 10 Å above the surface, beyond the range of the potential well. In order to represent a specific surface temperature, a heating process is required for the iron surface to increase the kinetic energy of the system. Yan et al. [45] showed that the phase change temperature obtained with MD simulations depends on the used heating process. Therefore, if the surface is expected to be in a solid phase, it is heated for 30 ps using the canonical (NVT) ensemble. To keep a constant temperature in the NVT ensemble simulations, the Nose-Hoover thermostat is applied on the translational degrees of freedom of the atoms with a temperature damping period of 100 fs. The warmed surfaces are then allowed to run first in the NVT ensemble and then in the micro-canonical (NVE) ensemble for 5 ps after which their state is saved to a file. If the surface is expected to be in a liquid phase, the surfaces are warmed using the Nose-Hoover thermostat for 30 ps to 2800 K, equilibrated for 5 ps at 2800 K and then gradually cooled down to the target temperature within 10 ps. Six different surfaces, each with different initial velocities, are generated to obtain a statistically meaningful set of data. Then, incident gas molecules are introduced with their velocities sampled from the Maxwell–Boltzmann (MB) distribution. 500

cases per warmed surface are sampled, which result in 3000 data points per configuration. The equations of motion are advanced using the Verlet algorithm with a timestep of 1 fs.

The interactions between the iron atoms are modeled using the embedded atom method (EAM) potential. The EAM force fields are based on the principle of embedding atoms within an electron cloud. The EAM potential reads

$$U_i = \frac{1}{2} \sum_{j \neq i} U_2 \left(r_{ij} \right) - F \left(\sum_{j \neq i} \rho_j \left(r_{ij} \right) \right), \tag{28}$$

where U_2 is a pairwise potential between atoms i and j, r_{ij} is the distance between atoms i and j, F is the embedding function, and ρ_j is the contribution to the electron charge density from atom j. Sipkens and Daun [32] investigated the effect of different surface potentials on the characteristics of an iron lattice, and found that the EAM potential of Zhou et al. [46] is the most robust choice since this potential well predicts the phase transitions and experimentally measured densities. Therefore, this work uses the EAM potential of Zhou et al. [46] for the iron surface potentials.

The gas-surface pairwise potentials are described by the Morse potential

$$U_{ij} = D_0 \left(1 - e^{-\alpha(r-r_0)} \right)^2, \tag{29}$$

where r_0 is the equilibrium bond distance and α controls the width of the potential.

Daun et al. [7] demonstrated the significance of using a well-defined gas-surface potential. They compared the TAC calculated with a Lennard–Jones 6–12 gas-surface potential with parameters derived from the Lorentz–Berthelot (LB) combination rules to the TAC calculated with a Morse potential with parameters derived from *ab initio* technique. For the LJ potential with LB combination rules, the well depth D_0 and finite distance σ were calculated by combining these values of the two individual atoms. For the *ab initio* calculations a molecule was moved towards a surface and then the potential was calculated from first principles. Daun et al. [7] showed that the TAC is overestimated when using a Lennard–Jones 6–12 gas-surface potential with parameters derived from the Lorentz–Berthelot (LB) combination rules, but found a good agreement with the values obtained from experiments when using a Morse potential with parameters derived from *ab initio* technique. The *ab initio* calculations for the Fe–N$_2$ interaction were performed by Sipkens et al. [33]. They found $D_0 = 2.162$ meV, $\alpha = 0.932$ Å^{-1} and $r_0 = 4.819$ Å.

3.3. Fe$_x$O$_y$-O$_2$ interaction

Different iron-oxide surfaces will be generated to investigate the effect of the oxidation stage of the iron-oxide surface on the TAC and MAC. The surface oxidation stage is denoted by the elemental mole fraction of oxygen in the particle and can be calculated as

$$Z_O = \frac{n_{O,s}}{n_{tot,s}}, \tag{30}$$

with $n_{O,s}$ being the number of oxygen atoms and $n_{tot,s}$ the total number of atoms in the complete domain. By means of this definition, Z_O remains constant in time if no new oxygen molecules are absorbed.

Before applying the Nose-Hoover thermostats, an FeO lattice is deposited in a specific ratio on top of a BCC lattice of Fe atoms. An initial distance of 4 Å between the two layers is introduced to ensure a natural mixing. The height of the FeO lattice compared to the Fe lattice is increased to increase the Z_O of the specific surface. Two different heating strategies are used to investigate the effect of the distribution of oxygen atoms over the surface:
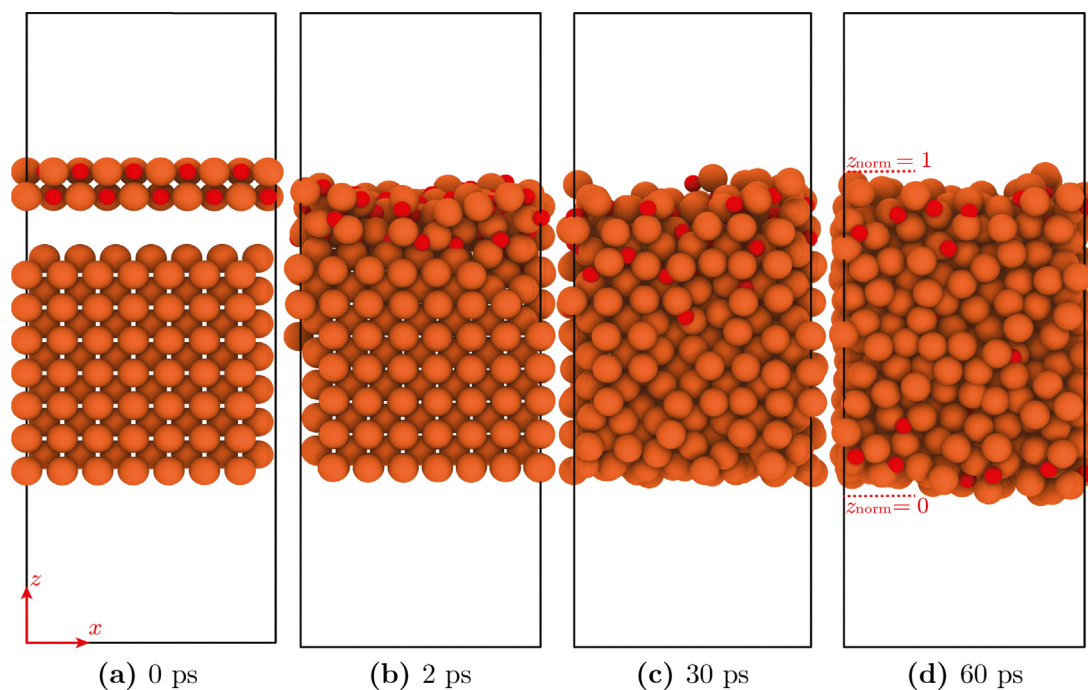
Fig. 3. Realization of an iron-oxide surface with $Z_O = 0.11$ and $T_p = 2000\,K$ for different moments in time during the preparation phase with heating strategy 1. The figures show a lateral surface, with the top surface used for the scattering gas molecule. Red particles represent oxygen atoms, while the brown particles are iron atoms. The sizes of the particles equal the atomic radii. In (d), the normalized z-positions are indicated. CPK coloring is used to distinguish different chemical elements.

1. The same heating strategy previously discussed for the Fe surface is used, with a different heating strategy for a solid or liquid surface.
2. An annealing process is employed for all the surfaces to enhance the mixing of the O and Fe atoms. The surfaces are warmed using the Nose-Hoover thermostat for 30 ps to 2800 K, equilibrated for 30 ps at the same temperature and then gradually cooled down to the target temperature within 30 ps.

Figure 3 shows the preparation of an iron-oxide surface with $Z_O = 0.11$ and $T_p = 2000\,K$ via heating strategy 1. After the surface realization, an O_2 molecule is located around 10 Å above the surface, beyond the range of the potential well. Figure 4 shows the initial configuration used for the interaction between Fe_xO_y and O_2.

Reactive molecular dynamics is used to simulate the interaction between Fe_xO_y-O_2. Reactive MD uses reactive force fields to accurately describe bond formation and breaking. ReaxFF [9] is a bond order potential that describes the total energy of the system as

$$E_{\text{system}} = E_{\text{bond}} + E_{\text{over}} + E_{\text{under}} + E_{\text{val}} + E_{\text{tor}}$$
$$+ E_{\text{vdWaals}} + E_{\text{Coulomb}} + E_{\text{additional}}, \tag{31}$$

with E_{bond} the bond formation/breaking energy, E_{over} and E_{under} the over- and undercoordination energy penalties, E_{val} and E_{tor} are respectively the valence and torsion angle energies, E_{vdWaals} and E_{Coulomb} are the non-bonded van der Waals and Coulomb long-range interactions and $E_{\text{additional}}$ are additional correction terms. The atomic charges are computed at every timestep using the charge equilibration method. A time step of 0.1 fs is used, which is recommended for reactive MD simulations at high temperatures [16]. The timestep is held sufficiently small to capture all reaction events at high temperatures. Six different surfaces, each with different initial velocities, are generated to obtain a statistically meaningful set of data. Table 1 lists the inter-atomic potentials that are used in this work to model the various inter-atomic interactions.

Table 1
Inter-atomic potentials used for the different atom-atom pair for either the Fe–N_2 or Fe_xO_y - O_2 interaction.

Case	Atom-atom pair	Inter-atomic potential	Reference
Fe–N_2	Fe–Fe	EAM potential	[46]
Fe–N_2	N–N	Rigid rotor	[8]
Fe–N_2	Fe–N_2	Morse potential	[33]
Fe_xO_y–O_2	Fe–Fe	ReaxFF	[1]
Fe_xO_y–O_2	O–O	ReaxFF	[1]
Fe_xO_y–O_2	Fe–O	ReaxFF	[1]

4. Results of the molecular dynamics simulations

The results for the mass and thermal accommodation coefficients determined from MD simulations are discussed below. It is important to note here that the MD simulation results are to some extent limited by the available (reactive) force fields. In addition, results from different force fields could differ quantitatively. Therefore, care must be taken in the selection of the force field. The effect of the available reactive force fields on the predicted thermal expansion is examined and presented in the Supplementary Material. As a result, it is concluded that ReaxFF proposed by Aryanpour et al. [1] is suited to reproduce an FeO and Fe_3O_4 surface. Therefore, this reactive force field is used in this work.

4.1. Mass accommodation coefficients

The mass accommodation coefficient for iron with oxygen is investigated for different initial oxidation stages, ranging from $Z_O = 0$ to $Z_O = 0.57$, and three different surface temperatures, namely, $T_p = 1500, 2000$ and $2500\,K$, of which the latter two are in the liquid-phase regime. A gas temperature of $T_g = 300\,K$ is used. The distance between the two O atoms of the incident oxygen molecule is used as a metric for the MAC. If the inter-atomic distance becomes larger than $1.2\times$ the initial bond length, the incident oxy-
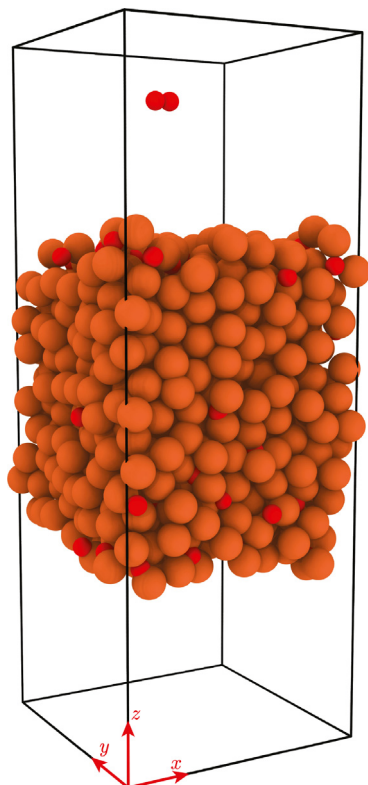
Fig. 4. Initial configuration showing an oxygen molecule (red particles) placed above a partially oxidized iron surface (brown particles) with $Z_O = 0.11$ and $T_p = 2000$ K. The sizes of the particles equal the atomic radii. CPK coloring is used to distinguish different chemical elements. (For interpretation of the references to colour in this figure legend, the reader is referred to the web version of this article.)

gen molecule is considered as dissociated, and chemically absorbed into the iron(-oxide) surface.

As discussed in Section 3.3, two different heating strategies are employed to investigate the effect of the non-uniform distribution of oxygen atoms in the surface. Figure 5 shows the probability density of oxygen atoms as a function of normalized z-position (as shown in Fig. 3(d)). For $T_p = 2000$ K, the oxygen atoms are characterized by a relatively uniform distribution, independent of the heating strategy. This lack of dependency is, however, not the case for $T_p = 1500$ K. With heating strategy 1 (HS1), the oxygen atoms are not uniformly distributed—a higher concentration is observed near the top surface. Because of the heating rate of HS1, not all of the oxygen atoms are sufficiently diffused to reach a uniform distribution. As a result, more oxygen atoms are near the surface. When the annealing process of HS2 is used, a spatially more uniform distribution of oxygen atoms is obtained.

Figure 6(a) shows the MAC of oxygen as a function of initial oxidation stage for the three different surface temperatures, obtained with HS2, while Fig. 6(b) shows a detailed view around $Z_O = 0.57$. To show the effect of a higher oxygen concentration at the top surface, the MAC obtained with HS1 for $T_p = 1500$ K is added to Fig. 6(a) as a red line. With a homogeneously distributed surface obtained via HS2, the MAC barely depends on the surface temperature and decreases as a function of Z_O. A fast decrease in MAC with increasing Z_O is observed if $Z_O < 0.5$, whereas the decrease of MAC becomes weaker for $Z_O > 0.5$. This result indicates that once the particle reaches stoichiometric FeO, it becomes more difficult to absorb oxygen.

As depicted in Fig. 6(a) with the red line, the MAC decreases significantly if there are more oxygen atoms near the surface. This accumulation at the top surface prevents new oxygen atoms from

being accommodated, indicating that the mass accommodation coefficient is affected by the local oxygen concentration near the surface. Thus, in this region the MAC is affected by a separation of time scales: The time period over which a gas molecule interacts with the surface is much shorter than the time period over which local oxygen concentration near the surface changes. Therefore, if the iron particle does not have a spatially uniform composition, internal transport may limit the oxidation rate of iron particles.

4.2. Thermal accommodation coefficients

4.2.1. Fe–N$_2$ interactions

The TAC for the Fe–N$_2$ interaction is investigated for different surface temperatures and a gas temperature of $T_g = 300$ K. An initially rough surface was created by projecting iron atoms on the initial smooth lattice. It is found that the TAC for the Fe–N$_2$ interaction is almost independent of temperature and equals $\alpha_T = 0.17$. These values are consistent with the values experimentally obtained by Sipkens et al. [33], who reported a value of 0.10 and 0.17. The effect of surface roughness on the TAC is discussed in the Supplementary Material.

In addition to the surface temperature of iron, the temperature of the surrounding gas can change significantly during iron combustion. Daun [6] and Mane et al. [21] investigated the effect of gas temperature on the TAC of nitrogen with soot and hydrogen with aluminum, respectively. They showed that the TAC is almost independent of gas temperature and primarily influenced by surface roughness and gas molecular weight. Based on the current MD results, a recommended value for the TAC of the interaction between Fe with N$_2$ equals 0.17.

4.2.2. Fe$_x$O$_y$–O$_2$ interactions

The oxygen molecules that do not stick to the surface during Fe$_x$O$_y$-O$_2$ interactions still contribute to the TAC. Figure 7 shows the total thermal accommodation coefficients of the Fe$_x$O$_y$-O$_2$ interaction as a function of Z_O at three different surface temperatures and a gas temperature of $T_g = 300$ K. When the oxidation degree of the surface is low, the TAC remains close to unity but decreases sharply to 0.2 once $Z_O > 0.5$. This trend can be explained by means of the number of hits that the incoming oxygen molecule has with the iron(-oxide) surface. With an increasing Z_O, the probability in number of hits decreases since the incoming oxygen is repelled by the surface. In other words, in a case with a larger Z_O, the oxygen molecule spends less time in contact with the surface, and therefore does not have the opportunity to equilibrate with the surface, resulting in a lower thermal accommodation coefficient. Note that, if Z_O is small, and thus MAC is large, the amount of scattered oxygen atoms over which the TAC is calculated is low. Since the total thermal accommodation coefficient is calculated with Eq. (27), however, this uncertainty in the low Z_O regime could be neglected due to the small contribution of α_{T,O_2} given by the large MAC number.

4.3. Discussion of the MD results

A limitation of the herein used molecular dynamics approach to determine the TAC and MAC is the assumption of a clean surface. Within experiments, surfaces could be (partly) covered by a layer of gas molecules. Song and Yovanovich [34] proposed a semi-empirical correlation for the TAC of engineering surfaces, which takes into account this absorbed layer. They state that the correlation is general and can be used for any combination of gases with a solid surface over a wide temperature range. However, Song and Yovanovich [34] state that a common strategy to create an adsorption-free surface within experiments is to heat the surface to high temperatures above 1000 K to desorb all of the impurities
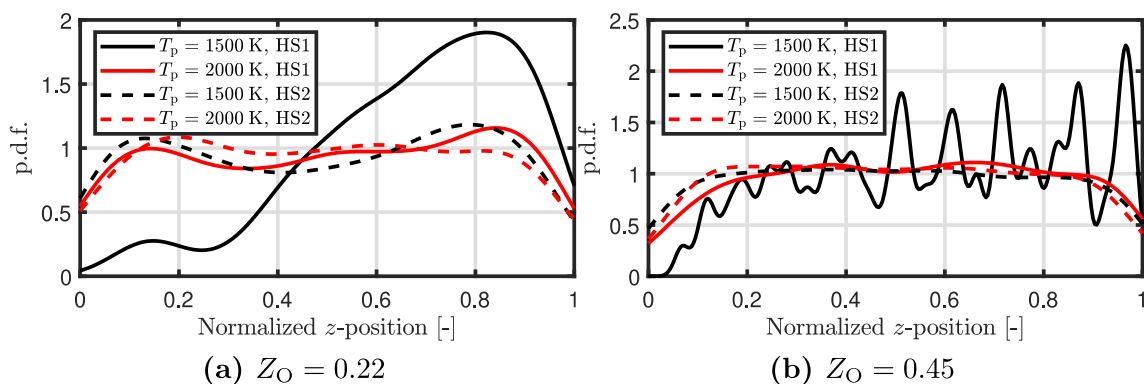
Fig. 5. Probability density function of oxygen atoms z-position for two different heating strategies, T_p and Z_O.
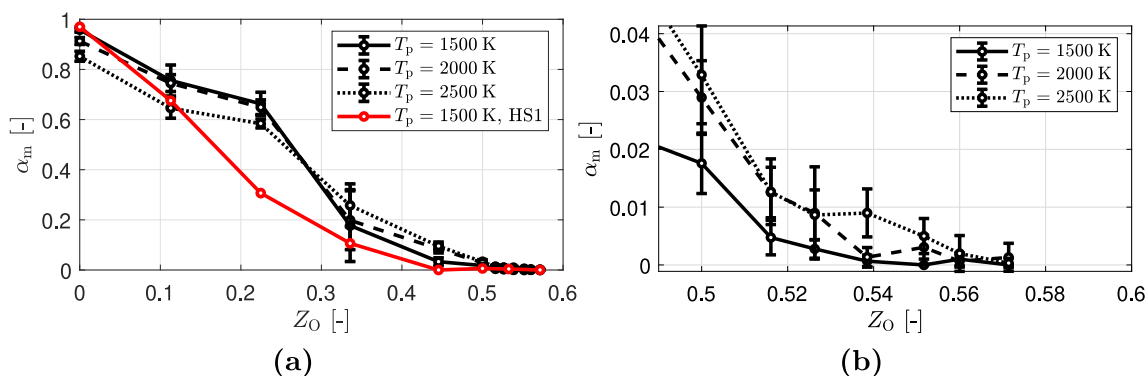

Fig. 6. The mass accommodation coefficient of oxygen as a function of initial oxidation stage at three different surface temperatures and $T_g = 300$ K. A detailed view around $Z_O = 0.5$ is shown in (b).

in the surface. The present work is mainly focused on the accommodation coefficients in the liquid-phase regime. Since the current MD simulations better represent the condition of a liquid-phase surface rather than a solid-phase surface with intrinsic roughness, the resulting accommodation coefficients in the temperature range above the melting points are likely more accurate. Jean-Philyppe et al. [15] used the correlation for the TAC as proposed by Song and Yovanovich [34] to investigate the ignition of iron particles in the Knudsen transition regime. A comparison between the TAC of the Fe-N_2 interaction obtained with the MD simulations compared to the semi-empirical correlation of Song and Yovanovich [34] is presented in the Supplementary Material. The TAC of Song and Yovanovich [34] is about three times larger than the TAC obtained with the molecular dynamics simulations.
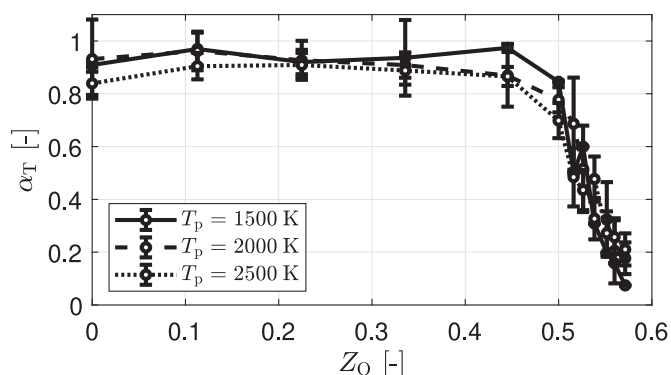
Nejad et al. [25] performed molecular dynamics simulations to investigate the influence of gas-wall and gas-gas interaction on different accommodation coefficients. They used a parallel wall approach to determine the accommodation coefficients, indicating that an intermediate Knudsen number is modeled. They showed that neglecting the gas-gas interaction results in lower TAC values with respect to the parallel wall approach: The TAC could be around 1.5 times larger if the gas-gas interaction effect were included [25]. However, in the two-layer model used in this work, a free-molecular regime is assumed within the Knudsen layer, implying that each incoming gas molecule does not interact with each other. Therefore, the accommodation coefficients obtained when neglecting the gas-gas interactions are consistent with the used two-layer model.

4.4. Implementation of the MD results in the single iron particle combustion model

The TAC and MAC obtained from the MD simulations are used in the single iron particle combustion model. In the iron particle model, it is assumed that the particle has a homogeneous mixture, such that there is no internal gradient in oxygen concentration. Therefore, the TAC and MAC values for Fe_xO_y-O_2 interactions are used from HS2, which are a function of Z_O and nearly independent of the surface temperature. In Table 2 the TAC and MAC for the Fe_xO_y-O_2 interactions are listed and averaged over the three surface temperatures. Within the iron particle combustion model, these values are used for linear interpolation. However, if no further oxidation is modeled after reaching the stoichiometry of FeO, a linear fit ($MAC_{Z_O<0.5} = -1.8Z_O + 0.9$) is used for the MAC such that $\alpha_m = 0$ if $Z_O = 0.5$. Eq. (27) describes the total TAC with $\alpha_{T,N_2} = 0.17$ and $\alpha_{T,O_2} = f(Z_O)$.

Fig. 7. Total thermal accommodation coefficients of the Fe_xO_y-O_2 interaction as a function of Z_O at three different surface temperatures, with $T_g = 300$ K.

Table 2

TAC and MAC for the Fe_xO_y–O_2 interactions, averaged over the three phase temperatures.

Z_O	0	0.11	0.22	0.34	0.45	0.5	0.52	0.53	0.54	0.55	0.56	0.57
α_m	0.908	0.716	0.632	0.211	0.071	0.027	0.010	0.007	0.004	0.003	0.001	0.001
α_T	0.893	0.946	0.919	0.911	0.903	0.774	0.557	0.517	0.371	0.265	0.207	0.154
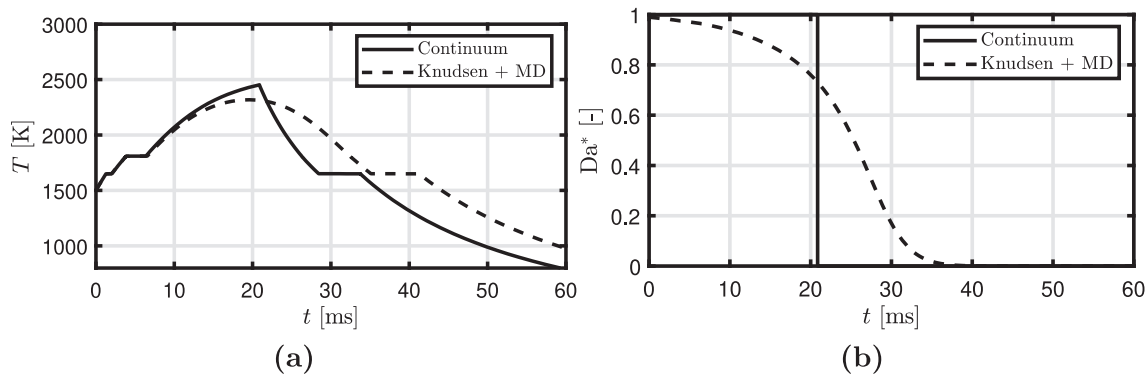
Fig. 8. (a) Temperature profile and (b) normalized Damköhler number for an iron particle of 50 μm burning at 21% oxygen concentration. The continuum model is compared to the MD-informed Knudsen model.

5. Results of single iron particle combustion simulations

In this section, the results of the MD-informed Knudsen model for a single iron particle burning in an O_2-N_2 atmosphere are presented. An initial particle temperature just above the ignition temperature, $T_{p,0} = 1100\,K$ [23], is considered.

5.1. Combustion behavior

First, the effect of the new model by only considering the first oxidation stage up to $Z_O = 0.5$ is investigated. The initial conditions are chosen such that the laser-ignited experiments performed by [26] are mimicked. A cold gas of $T_{g,0} = 300\,K$ at 1 atm is considered. The temperature profiles are shifted such that the particle temperature equals $T_{p,0} = 1500\,K$ at $t = 0\,ms$ [27].

Figure 8(a) shows the comparison of the temperature profiles between the continuum model and the MD-based Knudsen model for a 50 μm particle burning in $X_{O_2} = 0.21$. The temperature vs. time curve for the MD-informed Knudsen model changes significantly compared to the previously used continuum model. This difference can be explained by examining the Z_O value and heat transfer rates plotted in Fig. 9. In the continuum model, the maximum temperature was located at the position where $Z_O = 0.5$ is reached. At that time, the available iron is completely oxidized, and therefore the heat release rate immediately drops to zero. With

the MD-based Knudsen model, this behavior changes and $Z_O = 0.5$ is reached after the peak temperature. Since the rate of oxidation slows down, as the MAC decreases with an increasing oxidation stage, the rate of heat loss exceeds the rate of heat release upon reaching the maximum temperature of the particle, while the particle is not yet oxidized to $Z_O = 0.5$.

With the continuum model, it was discussed that the particle burns in a regime limited by the external diffusion of oxygen prior to the maximum temperature. One can derive a normalized Damköhler number Da^*. If Da^* is close to zero, the particle burns in a kinetic- (or chemical-) absorption-limited regime, and if it is close to unity, the particle burns in an external-diffusion-limited regime. Figure 8(b) shows the normalized Damköhler number for the same configuration. The normalized Damköhler number of the continuum model is determined according to the definition of Hazenberg and van Oijen [13]. For the Knudsen + MD model, the normalized Damköhler number is defined as

$$Da^* = 1 - \frac{\alpha_m X_{O_2,\delta}}{X_{O_2,g}},\qquad(32)$$

where $\alpha_m X_{O_2,\delta}$ denotes the molar fraction of oxygen at the particle surface $X_{O_2,p}$. As discussed before, with the continuum model the particle burns completely in an external-diffusion-limited regime prior to the maximum temperature. This behavior changes in the MD-informed Knudsen model: Due to the decreasing MAC value
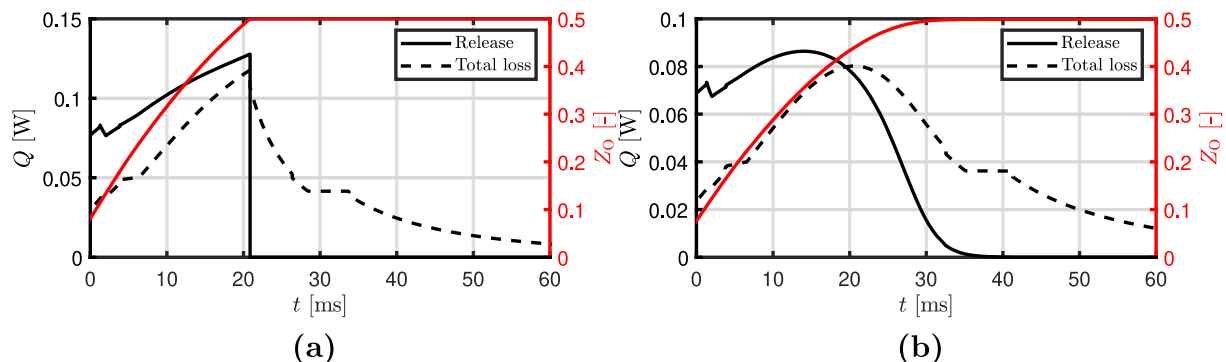
Fig. 9. Heat release and heat loss rates (left axis) and Z_O (right axis) for an iron particle of 50 μm burning at 21% oxygen concentration. The results are shown for (a) the continuum model and (b) the MD-informed Knudsen model.
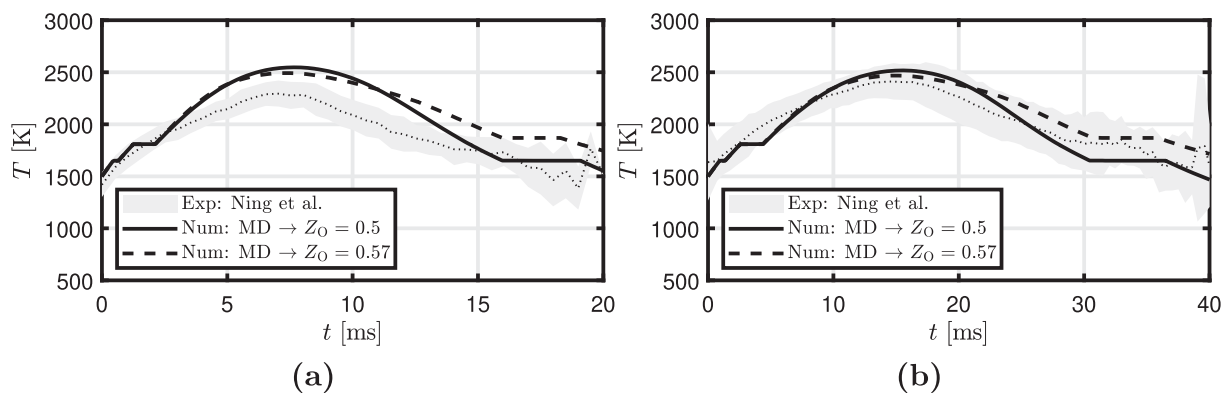
Fig. 10. Temperature profile for an iron particle of (a) 34 μm and (b) 50 μm burning at 26% oxygen concentration, with and without further oxidation beyond $Z_O = 0.5$. The dotted line and gray area are the mean and standard deviation of measurements obtained with the setup of Ning et al. [26], respectively.

with an increasing oxidation stage, the particle burns in an intermediate regime.

5.2. Comparison with experimental results

In [40,41], only the first stage of combustion, which is the oxidation to $Z_O = 0.5$, was investigated. Due to this assumption, an inert cooling stage was observed after the peak temperature. However, Choisez et al. [5] investigated combusted iron powders and discovered that it primarily consisted of a magnetite and hematite mixture, indicating a Z_O greater than 0.5. With the MD-informed Knudsen model, the oxidation beyond $Z_O = 0.5$ can be included in the combustion of a single particle.

The results of the MD-informed Knudsen model are compared with two sets of experimental data. First, the model is compared to the laser-ignited experiments of Ning et al. [27] wherein the particles burn in air at 300 K. Then, the new temperature curve is compared to the drop-tube experiments of Panahi et al. [28] wherein the particles burn in varying oxygen concentrations at 1350 K. The experimental data are averaged over multiple independent single-particle measurements to obtain a smooth curve.

5.2.1. Comparison with Ning et al.

Figure 10 shows the temperature profiles for the MD-informed Knudsen model with and without further oxidation beyond $Z_O = 0.5$ for a 34 μm and 50 μm particle burning in air with $X_{O_2} = 0.26$. The dotted line and gray area in Fig. 10 are the mean and standard deviation of the experimentally obtained temperature profiles, respectively.

The particle temperature for smaller particles is overestimated. Overall, the temperature curve obtained with the MD-informed Knudsen model shows a better agreement with the experimentally obtained temperature curve in contrast to the less smooth curve obtained with the external-diffusion limited continuum-model prediction, as shown in Fig. 8. The sharp transition at the peak temperature is now a smooth curve. The inclusion of the oxidation beyond $Z_O = 0.5$ results in a higher temperature in the tail of the curve. Instead of inert cooling after $Z_O = 0.5$, a reactive cooling regime is observed. The new numerically obtained slopes after the peak temperature qualitatively better agree with the experimental measurement during the cooling stage.

5.2.2. Comparison with Panahi et al.

Figure 11 shows the temperature profiles for the MD-informed Knudsen model with further oxidation beyond $Z_O = 0.5$ for a 49 μm particle burning in air with $X_{O_2} = 0.21$, 0.5 and 0.99. The dotted line and gray area are the mean and standard deviation of

experimentally obtained temperature profiles, respectively, which are calculated via the setup described by Panahi et al. [28]. Note that the effect of the Stefan flow correction on the evaporation rate is not taken into account. The data of Panahi et al. [28] are time-shifted so that the first experimental data point approximates the numerical temperature.

Although the model overestimates the particle temperature at the two higher oxygen concentrations, the agreement after the maximum temperature is reasonable. The reactive cooling slope which is observed after the maximum particle temperature seems to match the experimentally observed slope. This qualitative agreement implies that the oxidation process of the particle continues after the maximum particle temperature is reached.

A possible explanation for the overestimation of the particle temperature at higher oxygen concentrations could be due to assumption of a homogeneous mixture with infinitely fast internal transport for cases with these high oxygen concentrations. As shown in Section 4.1, the mass accommodation coefficient significantly decreases when the particle does not have a homogeneous composition, but a higher concentration of oxygen atoms near the surface. An inhomogeneous internal particle structure could arise from the miscibility gap between liquid iron (L1) and liquid iron-oxide (L2) [14] or due to the slow diffusion of oxygen in the condensed phase. Since for high oxygen concentrations in the gas, the external diffusion of oxygen is fast, the diffusion of oxygen in the condensed phase could be rate-limiting. With an increasing oxidation stage Z_O and an increased oxygen concentration X_{O_2} in the gas phase, internal transport could limit the absorption rate of new oxygen molecule, and therefore limit the maximum particle temperature. Further (experimental) research is needed to investigate the internal particle structure achieved during liquid iron particle combustion. Another possible explanation is that the current point-particle model is not valid in case of these extreme conditions. While it is already taken into account that the evaporated gaseous iron(-oxide) will further oxidize, and therefore inhibit the oxygen diffusion towards the particle, more components must be taken into account. The dense nano-particle cloud surrounding the particle can to some extent affect the boundary layer. Therefore, the validity of Eq. (14) must be reconsidered. On the one hand, including gas-phase reactions will enhance the evaporating flux, since gaseous iron will immediately oxidize and is therefore consumed. On the other hand, a strong Stefan flow induced by the surface chemisorption of oxygen would inhibit evaporation. Furthermore, how the nano-particle cloud affects the heat transfer in the boundary layer is also not taken into account in the current point-particle model. In [40] boundary-layer resolved simulations are performed to validate the current point-particle model, but
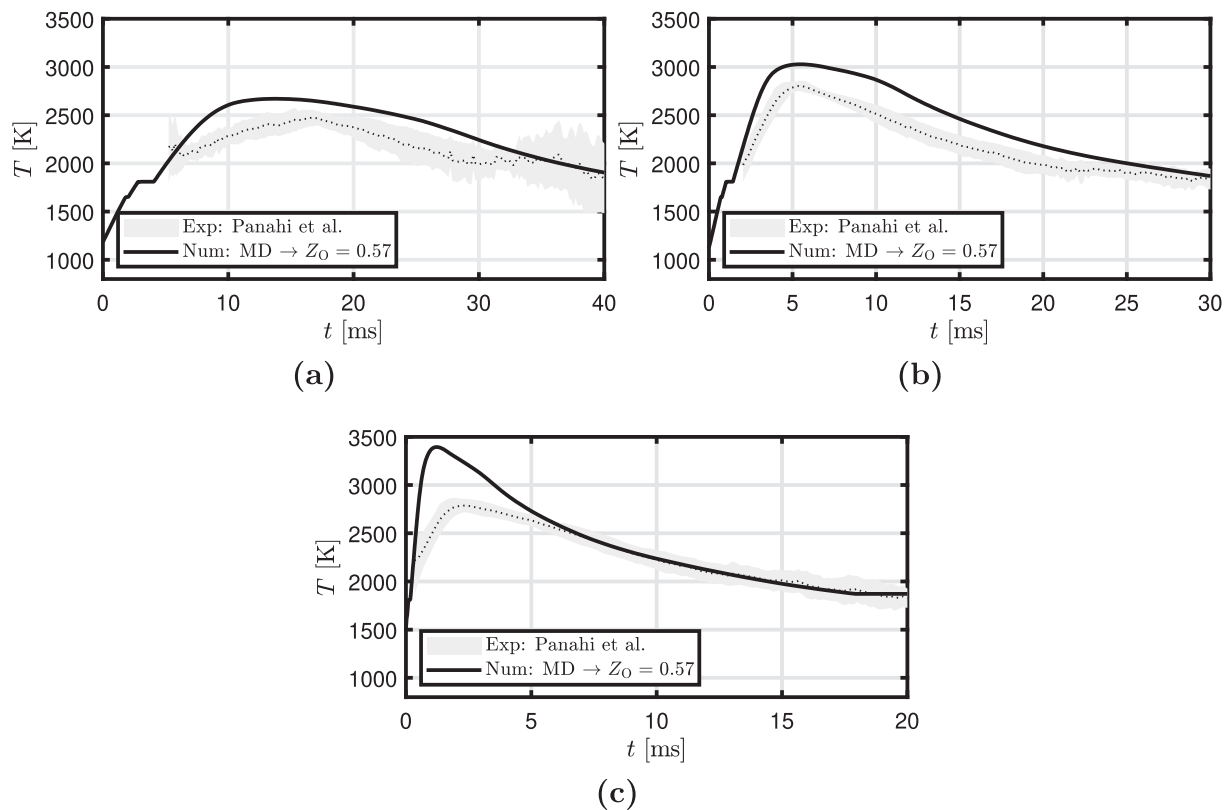
Fig. 11. Temperature profile for an iron particle of 49 μm burning at (a) 21%, (b) 50% and (c) 99% oxygen concentration. The dotted line and gray area are the mean and standard deviation of measurements obtained with the setup of Panahi et al. [28], respectively.

only simulations for relatively low oxygen concentrations are performed, without gas-phase kinetics. To validate the current point-particle model, boundary-layer resolved simulations at these high oxygen concentrations must be performed to investigate the validity of the current point-particle model under these extreme conditions.

5.3. Effect of α_T and α_m

The results of the molecular dynamics simulations are dependent on the accuracy of the inter-atomic potentials and, perhaps, also on the configuration. Related changes in the TAC and MAC have an effect on the temperature profile during combustion. In this section, the TAC and MAC are varied independently to investigate the effect on the combustion behavior.

As discussed in Section 4.3, the TAC could be around 1.5 times larger if gas-gas interactions are taken into account. Although neglecting the gas-gas interaction in the current case is justified, this extreme variation of 50% is used in this section to independently vary the TAC and MAC, with a maximum value of 1. Figure 12 shows the effect on the temperature profile and Z_O for a 10 μm and 50 μm particle burning in $X_{O_2} = 0.21$ and with $T_g = 300$ K. Both α_T and α_m have a significant effect on the particle temperature. For the 10 μm particle, the maximum temperature could vary by 200 K due to the variations of α_T and α_m, while for the 50 μm particle the variation is around 130 K. The effect is more significant for the smaller particles, since they are more dominated by the free-molecular heat and mass transfer.

An increasing α_T results in a lower particle temperature, while the opposite is seen for a decreasing α_T. With an increasing α_T, the exchange of kinetic energy between the gas molecules and the surface is more efficient, resulting in a greater rate of heat loss

and therefore a decreasing particle temperature. A variation in α_T hardly affects the oxidation rate.

A variation in α_m affects both the temperature profile as well as the oxidation stage Z_O. An increasing α_m results in a faster oxidation rate for the iron particle, leading to a faster heat release and therefore an increase in particle temperature. Note that the variation is relative, and thus the absolute difference with respect to the original values becomes smaller when α_m is close to zero.

5.4. Effect of transition modeling on the burn time

The effect of the transition regime on the temperature profile of a variety of particles burning in $X_{O_2} = 0.21$ and with $T_g = 300$ K is investigated. Figure 13 shows the difference for the time to maximum temperature t_{max} obtained with either the continuum and transition model as a function of particle diameter. Only the oxidation to $Z_O = 0.5$ is considered for the MD-informed Knudsen model. Here, t_{max} is the time elapsed from $T_{p,0} = 1100$ K to T_{max}. Due to the large difference in values for t_{max}, the relative difference with respect to the continuum model is plotted. The error bars show the effect of varying both α_T and α_m by 50%.

When using the MD-informed Knudsen model, it is clear that the time to maximum temperature increases for smaller particles. Since the free-molecular regime inhibits mass transfer towards the particle, t_{max} increases. However, with an increasing particle size, the new t_{max} value becomes smaller than with the continuum model. This result is recognized as an effect of the decreasing MAC with an increasing Z_O. A critical diameter $d_{p,c}$ is defined, which means that if $d_p < d_{p,c}$, it is important to include the transition regime. For $d_{p,c}$ we define that if one considers $t_{max}/t_{max,co} < 1.10$ as the criterion, critical particle size is found to be $d_{p,c} \approx 15$ μm. This criterion suggests that, if one uses a continuum-based model
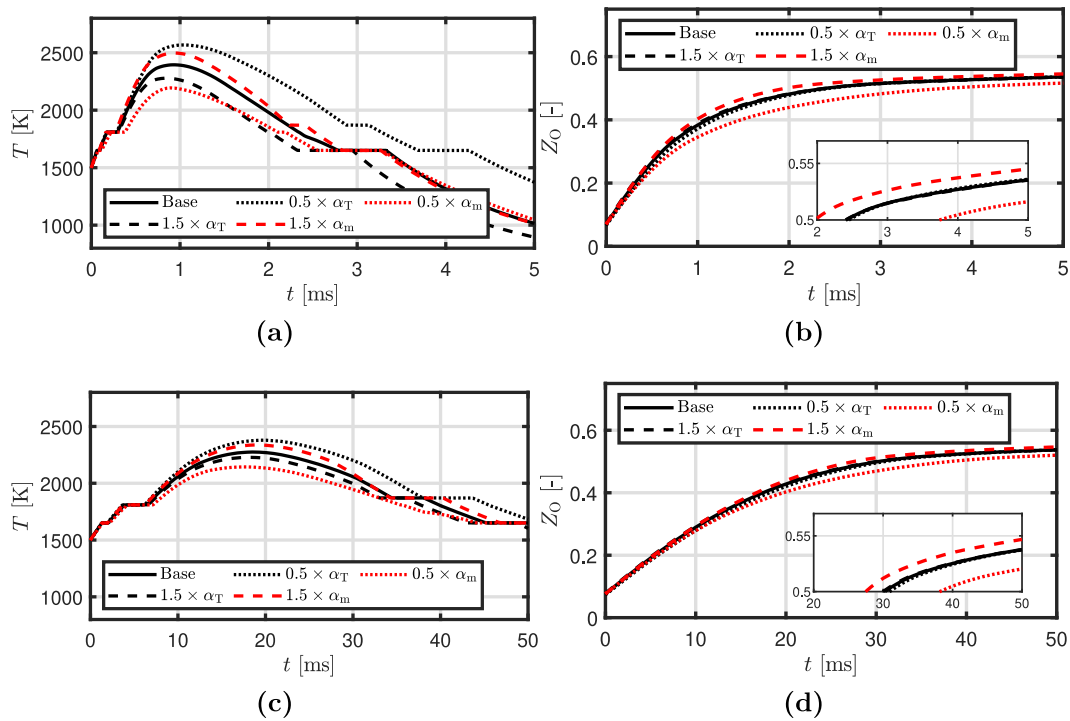
Fig. 12. The effect of changes in α_T and α_m for a iron particle of (a) + (b) 10 μm and (b) + (c) 50 μm burning at 21% oxygen concentration. (a) + (c) The particle temperature and (b) + (d) Z_O.

to describe the combustion of iron particles smaller than 10 μm, the burn time can be underestimated by more than 10% due to neglecting the effects of transition-regime transport phenomena.

5.5. Effect of particle size on the maximum temperature

Figure 14 shows the maximum temperature (T_{max}) as a function of the particle size, obtained with either the MD-informed Knudsen model or the continuum model. The conditions are $X_{O_2} = 0.21$ and $T_g = 300$ K. T_{max} as a function of particle size changes with respect to the continuum model. It is hard to distinguish any transition regime effects in this curve since due to the decreasing MAC with increasing Z_O, the maximum temperature already decreased with respect to the continuum model. Ning et al. [27] observed a decreasing maximum particle temperature with a decreasing particle size in the range of 25–54 μm. Panahi et al. [28] did not observe the effect of particle size on the maximum temperature in the particle size range of 38–53 μm. Judging from the PSD (particle

size distribution) used by Panahi et al. [28], namely 38–45 μm and 45–49 μm, the particle samples did not differ significantly in diameter. To ensure that these distributions are not overlapping and thereby altering the influence of the particle size on the maximum temperature, a more comprehensive description of the PSD's used in the studies would be required.

In the present work, an even opposite trend is observed: The maximum temperature decreases with increasing particle size. Since both the amount of potential heat release and thermal inertia scale with d_p^3, the d_p vs. T_{max} trend can be predicted and explained by examining how the heat release rate $\dot{Q}_r$ and heat loss rate $\dot{Q}_l$ scale with the particle size d_p (denoted as $\dot{Q}_i(d_p)$). If the heat loss rate increases faster with particle size than the heat release rate, then the maximum temperature will decrease with an increasing particle size. If the heat release rate increases faster with increasing particle size than the heat loss rate, then the maximum temperature will increase. To obtain the decreasing maximum particle temperature with a decreasing particle size trend,
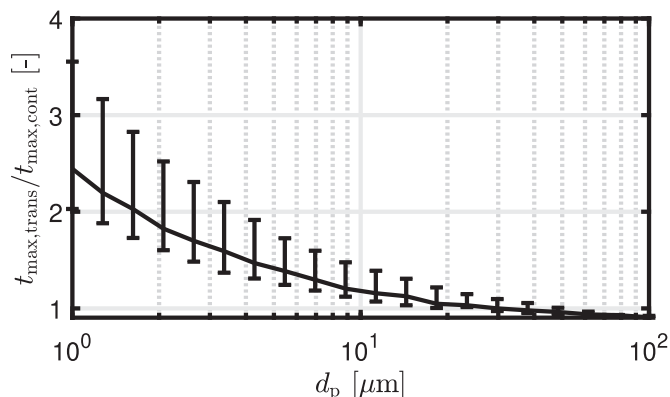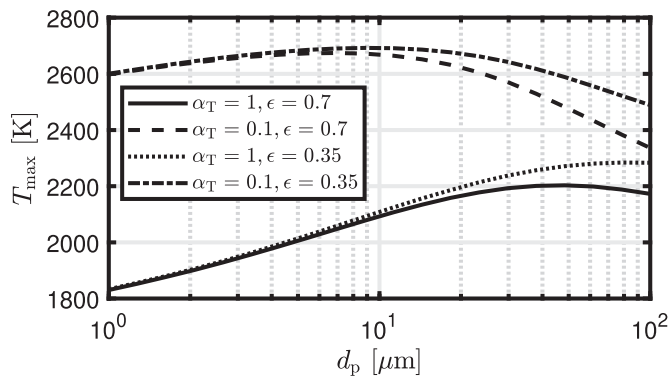

Fig. 13. The effect of the MD-informed Knudsen model compared to the continuum model for $t_{max}/t_{max,co}$. Values are obtained with $X_{O_2} = 0.21$.
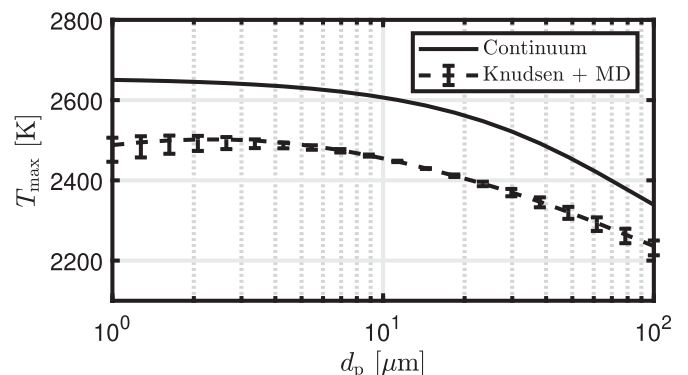
Fig. 14. The effect of the MD-informed Knudsen model compared to the continuum model for T_{max}. Values are obtained with $X_{O_2} = 0.21$.

Fig. 15. The effect of the MD-informed Knudsen model compared to the continuum model for T_{max}. Values are obtained with $X_{O_2} = 0.21$.

the following inequality must hold

$$\frac{\int_{t_0}^{t_{max}} \dot{Q}_r(d_p)\, dt}{\int_{t_0}^{t_{max}} \dot{Q}_l(d_p)\, dt} > 1. \tag{33}$$

In completely external-diffusion-limited continuum models neglecting the effects of slip velocity and radiation, both the heat release rate and the heat loss rate scale with d_p (See Eqs. (14) and (15)). Therefore, $\frac{\dot{Q}_r}{\dot{Q}_l} \propto \frac{d_p}{d_p} = 1$ and no particle size effect on the maximum temperature is expected. A slip velocity will affect how T_{max} scales with d_p since it affects both the Sherwood and Nusselt numbers, which have an impact on $\dot{Q}_r$ and $\dot{Q}_l$. Since for air the Lewis number is slightly larger than 1, it holds that $Sc > Pr$ and therefore $Sh(d_p) > Nu(d_p)$. As a result, the maximum temperature will increase with particle size. However, since the Lewis number is nearly one, the impact is negligible. Ning et al. [27] argue that a larger particle has less radiation heat loss due to a smaller surface-to-volume ratio than a smaller particle. However, radiative heat loss scales with d_p^2 and thus total heat loss scales with d_p^m, with $m > 1$. So in the case of an external-diffusion-limited continuum model with radiation, $\frac{\dot{Q}_r}{\dot{Q}_l} \propto \frac{d_p}{d_p^m}$, which results in exactly the opposite trend as observed by [27]: The maximum temperature decreases as particle size increases. This explains why the maximum temperature in the model decreases as particle size increases.

Due to the inclusion of chemisorption, the particle is not completely external-diffusion-limited. This results in a heat release rate that does not scale linearly in d_p (as it would for a fully external-diffusion-limited particle), but instead scales as d_p^n, with $n > 1$. This effect could result in the inequality of Eq. (33). On the other hand, the impact of the free-molecular regime is a function of particle size. Therefore, this will also impact the heat release rate, so it holds

$$\frac{\dot{Q}_r}{\dot{Q}_l} \propto \frac{d_p^n}{d_p^m}. \tag{34}$$

The combined effect of chemisorption and transition-regime heat and mass transfer cannot be used to explain the lowering maximum particle temperature with a decreasing particle size trend.

To investigate the effect of particle size on the maximum temperature, a parametric study has been conducted. The maximum temperature vs particle size trend is affected by radiation and heat transfer in the Knudsen regime, as was previously stated. The TAC in this work is based on molecular dynamics simulations and is a function of Z_O, with $\epsilon = 0.7$ based on iron-oxide (L2) [24]. Figure 15 demonstrates a sensitivity analysis of the TAC and the emissivity. The emissivity is adjusted into the emissivity of liquid iron (L1) $\epsilon = 0.35$ [24], while the TAC is varied between $\alpha_T = 1$, and $\alpha_T = 0.1$. Only the region above 10 μm is impacted by the

changing emissivity because radiative heat loss only becomes substantial for larger particles. Variations in emissivity between 0.7 and 0.35 can lower the maximum temperature for the large particle of 100 μm by about 150 K. Small particles are affected significantly by changes in the thermal accommodation coefficient, with variations in the maximum temperature of about 800 K. Assuming the emissivity of liquid iron (L1) and assuming perfect thermal accommodation ($\alpha_T = 1$) will result in an increasing maximum temperature with increasing particle size trend. However, perfect accommodation for metal-gas interactions is not expected. Therefore, further research is required to explain and confirm the particle size effect on the maximum temperature.

6. Conclusions

Molecular dynamics simulations have been performed to investigate the thermal and mass accommodation coefficients for the combination of iron(-oxide) and air. The obtained relations for the TAC and MAC are used in a point-particle Knudsen model to investigate the effects on the combustion behavior of (fine) iron particles.

The TAC for the interaction of Fe with N_2 is almost independent of the surface temperature and equals $\alpha_T = 0.17$. For Fe_xO_y–O_2 interactions, the TAC remains close to unity when the oxidation degree of the surface is low, but decreases abruptly to 0.2 once it reaches the stoichiometry of FeO. The MAC decreases as a function of Z_O. A fast decrease is observed if $Z_O < 0.5$ and a weaker decrease if $Z_O > 0.5$. This trend indicates that once the particle reaches stoichiometric FeO, it becomes more difficult to absorb oxygen.

By incorporating the MD information into the single iron particle model, a new temperature-time curve for the single iron particles is observed compared to results obtained with previously developed continuum models. Since the rate of oxidation slows down as the MAC decreases with an increasing oxidation stage, the rate of heat release decreases when reaching the maximum temperature, such that the rate of heat loss exceeds that of heat release, while the particle is not yet oxidized to $Z_O = 0.5$. In addition, the oxidation beyond $Z_O = 0.5$ (from stoichiometric FeO to Fe_3O_4) is modeled. The effect of the transition-regime heat and mass transfer on the burn time becomes more than 10% if the particles are smaller than 15 μm.

In the cases with relatively high O_2 concentrations in the gasphase, the model overestimates the particle temperature. The reactive cooling slope observed after the maximum particle temperature, however, reasonably agrees with the experimentally observed slope. This overestimation could be attributed to either the assumption of a homogeneous mixture with infinitely fast transport of oxygen inside the particle or to the validity point-particle model itself. These are areas that should be further investigated in future work.

The results and findings of the present work provide new insights into the effects of the free-molecular regime and surface chemisorption on the oxidation of single iron particles that could open up more comprehensive models for fine iron particle oxidation.

Declaration of Competing Interest

The authors declare that they have no known competing financial interests or personal relationships that could have appeared to influence the work reported in this paper.

Supplementary material

Supplementary material associated with this article can be found, in the online version, at doi:10.1016/j.combustflame.2023.112871.

References

[1] M. Aryanpour, A.C.T. van Duin, J.D. Kubicki, Development of a reactive force field for iron-oxyhydroxide systems, J. Phys. Chem. A 114 (21) (2010) 6298–6307, doi:10.1021/jp101332k. PMID: 20455552

[2] J.M. Bergthorson, S. Goroshin, M.J. Soo, P. Julien, J. Palecka, D.L. Frost, D.J. Jarvis, Direct combustion of recyclable metal fuels for zero-carbon heat and power, Appl. Energy 160 (2015) 368–382.

[3] R.B. Bird, E.N. Lightfoot, W.E. Stewart, Transport phenomena, J. Wiley, 2002.

[4] V. Chirita, B. Pailthorpe, R. Collins, Molecular dynamics study of low-energy Ar scattering by the Ni(001) surface, J. Phys. D 26 (1) (1993) 133.

[5] L. Choisez, N.E. van Rooij, C.J. Hessels, A.K. da Silva, I.R.S. Filho, Y. Ma, P. de Goey, H. Springer, D. Raabe, Phase transformations and microstructure evolution during combustion of iron powder, Acta Mater. 239 (2022) 118261.

[6] K. Daun, Thermal accommodation coefficients between polyatomic gas molecules and soot in laser-induced incandescence experiments, Int. J. Heat Mass Transf. 52 (21) (2009) 5081–5089, doi:10.1016/j.ijheatmasstransfer.2009.05.006.

[7] K. Daun, J. Titantah, M. Karttunen, Molecular dynamics simulation of thermal accommodation coefficients for laser-induced incandescence sizing of nickel particles, Appl. Phys. B 107 (35) (2012) 221–228, doi:10.1007/s00340-012-4896-x.

[8] J.C. Decius, Relation between force constant and bond length for the nitrogen-nitrogen bond, J. Chem. Phys. 45 (3) (1966) 1069, doi:10.1063/1.1727664.

[9] A.C.T. van Duin, S. Dasgupta, F. Lorant, W.A. Goddard, ReaxFF: a reactive force field for hydrocarbons, J. Phys. Chem. A 105 (41) (2001) 9396–9409, doi:10.1021/jp004368u.

[10] G. Finger, J. Kapat, A. Bhattacharya, Molecular dynamics simulation of adsorbent layer effect on tangential momentum accommodation coefficient, J. Fluids Eng. 129 (1) (2006) 31–39.

[11] A. Fujinawa, L.C. Thijs, J. Jean-Philyppe, A. Panahi, D. Chang, M. Schiemann, Y. Levendis, J. Bergthorson, X. Mi, Combustion behavior of single iron particles—Part II: a theoretical analysis based on a zero-dimensional model, Appl. Energy Combust. Sci. 14 (2023) 100145.

[12] C.E.A.G. van Gool, L.C. Thijs, W.J.S. Ramaekers, J.G.M. Kuerten, J.A. van Oijen, L.P.H. de Goey, Particle equilibrium composition model for iron dust combustion, Prog. Energy Combust. 13 (2022) 100115.

[13] T. Hazenberg, J.A. van Oijen, Structures and burning velocities of flames in iron aerosols, Proc. Combust Inst. 38 (3) (2021) 4383–4390.

[14] T. Hidayat, D. Shishin, E. Jak, S.A. Decterov, Thermodynamic reevaluation of the Fe–O system, Calphad 48 (2015) 131–144, doi:10.1016/j.calphad.2014.12.005.

[15] J. Jean-Philyppe, A. Fujinawa, J. Bergthorson, X. Mi, The ignition of fine iron particles in the Knudsen transition regime (2022). 10.13140/RG.2.2.30880.05129

[16] E.M. Kritikos, A. Lele, A.C. van Duin, A. Giusti, A reactive molecular dynamics study of the effects of an electric field on n-dodecane combustion, Combust. Flame 244 (2022) 112238.

[17] L.C. Kröger, W.A. Kopp, M. Döntgen, K. Leonhard, Assessing statistical uncertainties of rare events in reactive molecular dynamics simulations, J. Chem. Theory Comput. 13 (9) (2017) 3955–3960, doi:10.1021/acs.jctc.7b00524.

[18] S. Li, J. Huang, W. Weng, Y. Qian, X. Lu, M. Aldén, Z. Li, Ignition and combustion behavior of single micron-sized iron particle in hot gas flow, Combust. Flame 241 (2022), doi:10.1016/j.combustflame.2022.112099.

[19] S. Li, D. Sanned, J. Huang, E. Berrocal, W. Cai, M. Aldén, M. Richter, Z. Li, Stereoscopic high-speed imaging of iron microexplosions and nanoparticle-release, Opt. Express 29 (21) (2021) 34465–34476.

[20] F. Liu, K.J. Daun, D.R. Snelling, G.J. Smallwood, Heat conduction from a spherical nano-particle: status of modeling heat conduction in laser-induced incandescence, Appl. Phys. B 83 (2006) 355–382.

[21] T. Mane, P. Bhat, V. Yang, D.S. Sundaram, Energy accommodation under non-equilibrium conditions for aluminum-inert gas systems, Surf. Sci. 677 (2018) 135–148, doi:10.1016/j.susc.2018.05.011.

[22] M. McRae, P. Julien, S. Salvo, S. Goroshin, D.L. Frost, J.M. Bergthorson, Stabilized, flat iron flames on a hot counterflow burner, Proc. Combust. Inst. 37 (3) (2019) 3185–3191, doi:10.1016/j.proci.2018.06.134.

[23] X. Mi, A. Fujinawa, J.M. Bergthorson, A quantitative analysis of the ignition characteristics of fine iron particles, Combust. Flame 240 (2022) 112011.

[24] M. Muller, H.E. Rabii, R. Fabbro, Liquid phase combustion of iron in an oxygen atmosphere, J. Mater. Sci. 50 (2015) 3337–3350.

[25] S.M. Nejad, S. Nedea, A. Frijns, D. Smeulders, The influence of gas–wall and gas–gas interactions on the accommodation coefficients for rarefied gases: amolecular dynamics study, Micromachines 11 (3) (2020) 319.

[26] D. Ning, Y. Shoshin, J.A. van Oijen, G. Finotello, L.P.H. de Goey, Burn time and combustion regime of laser-ignited single iron particle, Combust. Flame 230 (2021) 111424.

[27] D. Ning, Y. Shoshin, M. van Stiphout, J.A. van Oijen, G. Finotello, L.P.H. de Goey, Temperature and phase transitions of laser ignited single iron particle, Combust. Flame 236 (2021) 111801.

[28] A. Panahi, D. Chang, M. Schiemann, A. Fujinawa, X. Mi, J.M. Bergthorson, Y.A. Levendis, Combustion behavior of single iron particles—Part I: an experimental study in a drop-tube furnace under high heating rates and high temperatures, Appl. Energy Combust. Sci. 13 (2022) 100097.

[29] S. Peddakotla, K. Kammara, R. Kumar, Molecular dynamics simulation of particle trajectory for the evaluation of surface accommodation coefficients, Microfluid Nanofluidics 23 (6) (2019) 79.

[30] S. Roy, M. Hegde, G. Madras, Catalysis for NOx abatement, Appl. Energy 86 (11) (2009) 2283–2297, doi:10.1016/j.apenergy.2009.03.022.

[31] E.I. Senyurt, E.L. Dreizin, At what ambient temperature can thermal runaway of a burning metal particle occur? Combust. Flame 236 (2022) 111800, doi:10.1016/j.combustflame.2021.111800.

[32] T.A. Sipkens, K.J. Daun, Effect of surface interatomic potential on thermal accommodation coefficients derived from molecular dynamics, J. Phys. Chem. C 122 (35) (2018) 20431–20443, doi:10.1021/acs.jpcc.8b06394.

[33] T.A. Sipkens, N.R. Singh, K.J. Daun, N. Bizmark, M. Ioannidis, J.T. Titantah, M. Karttunen, Time resolved laser induced incandescence for sizing aerosolized iron nanoparticles, Heat Transfer and Thermal Engineering, vol. 8B, 2014, doi:10.1115/IMECE2014-38515.

[34] S. Song, M.M. Yovanovich, Correlation of thermal accommodation coefficient for engineering surfaces, ASME HTD 69 (1987) 107–116.

[35] M. Soo, X. Mi, S. Goroshin, A.J. Higgins, J.M. Bergthorson, Combustion of particles, agglomerates, and suspensions—A basic thermophysical analysis, Combust. Flame. 192 (2018) 384–400.

[36] M.J. Soo, K. Kumashiro, S. Goroshin, D.L. Frost, J.M. Bergthorson, Thermal structure and burning velocity of flames in non-volatile fuel suspensions, Proc. Combust. Inst. 36 (2) (2017) 2351–2358, doi:10.1016/j.proci.2016.06.043.

[37] J. Sun, Z. Li, Effect of gas adsorption on momentum accommodation coefficients in microgas flows using molecular dynamic simulations, Mol. Phys. 106 (19) (2008) 2325–2332.

[38] J.H. Sun, R. Dobashi, T. Hirano, Combustion behavior of iron particles suspended in air, Combust. Sci. Technol. 150 (2000) 99–114.

[39] F.-D. Tang, S. Goroshin, A. Higgins, J. Lee, Flame propagation and quenching in iron dust clouds, Proc. Combust. Inst. 32 (2) (2009) 1905–1912, doi:10.1016/j.proci.2008.05.084.

[40] L.C. Thijs, C.E.A.G. van Gool, W.J.S. Ramaekers, J.G.M. Kuerten, J.A. van Oijen, L.P.H. de Goey, Improvement of heat- and mass transfer modeling for single iron particles combustion using resolved simulations, Combust. Sci. Technol. 0 (0) (2022) 1–17, doi:10.1080/00102202.2022.2089030.

[41] L.C. Thijs, C.E.A.G. van Gool, W.J.S. Ramaekers, J.A. van Oijen, L.P.H. de Goey, Resolved simulations of single iron particle combustion and the release of nanoparticles, Proc. Combust. Inst. (2023), doi:10.1016/j.proci.2022.07.044.

[42] A.P. Thompson, H.M. Aktulga, R. Berger, D.S. Bolintineanu, W.M. Brown, P.S. Crozier, P.J. in 't Veld, A. Kohlmeyer, S.G. Moore, T.D. Nguyen, R. Shan, M.J. Stevens, J. Tranchida, C. Trott, S.J. Plimpton, LAMMPS - a flexible simulation tool for particle-based materials modeling at the atomic, meso, and continuum scales, Comput. Phys. Commun. 271 (2022) 108171, doi:10.1016/j.cpc.2021.108171.

[43] J. Thoudam, T. Mane, D. Sundaram, Effect of melting on energy accommodation coefficients of aluminum–noble gas systems, J. Phys. Chem. C 124 (40) (2020) 22105–22116.

[44] P. Tóth, Y. Ögren, A. Sepman, P. Gren, H. Wiinikka, Combustion behavior of pulverized sponge iron as a recyclable electrofuel, Powder Technol. 373 (2020) 210–219.

[45] H.-J. Yan, J.-C. Zhuang, P. Zhou, Q. Li, C.Q. Zhou, P. Fu, Molecular dynamics simulation of thermal physical properties of molten iron, Int. J. Heat Mass Transf. 109 (2017) 755–760, doi:10.1016/j.ijheatmasstransfer.2017.02.027.

[46] X.W. Zhou, R.A. Johnson, H.N.G. Wadley, Misfit-energy-increasing dislocations in vapor-deposited CoFe/NiFe multilayers, Phys. Rev. B 69 (2004) 144113, doi:10.1103/PhysRevB.69.144113.